Brazilian Journal of Geophysics
Brazilian Journal of Geophysics, **42** (2024), 1, 1–11
Brazilian Geophysical Society
ISSN 2764-8044
DOI 10.22564/brjg.v41i2.2305

A HIGH-RESOLUTION SUBTLE FAULT MAPPING IN MARLIN FIELD, BRAZIL

Leonardo Campos João[1], Paulo T. L. Menezes[2,*],
and Sergio Bergamaschi[3]

[1]Universidade do Estado do Rio de Janeiro - UERJ – PPGG, Rio de Janeiro, RJ, Brazil
[2]Universidade do Estado do Rio de Janeiro - UERJ, Dep. Geologia Aplicada, Rio de Janeiro, RJ, Brazil
[3]Universidade do Estado do Rio de Janeiro - UERJ, Dep. Estratigrafia e Paleontologia, Rio de Janeiro, RJ, Brazil

[*]Corresponding author: paulo.menezes@uerj.br

ABSTRACT. Discriminating geological discontinuities is important for reservoir management because they influence storage capacity and fluid flow. Structural heterogeneities, such as faults and fractures, significantly impact the compartmentalization of the reservoir facies and affect the flow of hydrocarbons. These structures can act as the pore space for fluid storage, flow-control conduits, or barriers that allow the accumulation of exploitable volumes of oil and gas. Understanding the spatial and temporal development of these structures can significantly impact hydrocarbon exploration. Reservoir characterization is a critical process in the oil and gas industry that aims to comprehensively understand reservoir rocks and their fluid content and distribution. It is a multidisciplinary approach that combines geological, geophysical, and engineering datasets through statistical and deterministic mathematical models. Seismic datasets play a crucial role in reservoir characterization. Interpreters can use seismic data processing and imaging to interpret geological horizons and map faults, building complex geological models. Seismic inversion is also employed to estimate acoustic impedance and other petrophysical properties. The mapping of faults and fractures integrates highly relevant themes in reservoir characterization. Identifying subtle faults and fractures is essential in specifying hydrocarbon migration paths and identifying bypassed oil accumulations. However, traditional seismic amplitude data interpretation should consider these structures more. In this study, we apply a high-resolution fault mapping workflow to map the subtle fault system in the Marlim field in the offshore portion of the Campos Basin. As an outcome, we imaged two separate fault trends inside and outside the Marlim reservoir.

Keywords: subtle fault mapping, seismic attributes, relative acoustic impedance, Marlim turbidites

INTRODUCTION

Determining geological discontinuities is critical for reservoir management, as they control storage space and fluid flow. Structural heterogeneities, such as faults and fractures, greatly modify the compartmentalization of the reservoir's facies, impacting the flow of hydrocarbons in a given reservoir. Such structures can act as the pore space for storing fluids, as flow-control conduits, and as barriers that allow the accumulation of exploitable volumes of oil and gas. In this way, understanding the spatial and temporal development of these structures can significantly impact hydrocarbon exploration.

Reservoir characterization is one of the leading processes in the oil and gas industry for delivering a comprehensive scenery of reservoir rocks and their fluid content and distribution. It is a multidisciplinary procedure merging geological, geophysical and engineering datasets via statistical and/or deterministic mathematical models (Grana et al., 2021).

Seismic datasets are essential to reservoir characterization. Interpreters can interpret geological horizons and map faults through seismic data processing and imaging to build complex geological models. And, by employing seismic inversion, it is possible to calculate acoustic impedance and other petrophysical properties (Carvalho and Menezes, 2017; Lupinacci et al., 2020).

The mapping of faults and fractures integrates themes of huge relevance in reservoir characterization. Identifying subtle faults, i.e., those with small offsets close to or below the seismic tuning thicknesses, and fractures plays an important role in specifying hydrocarbon migration paths and bypassed oil accumulations (Hussein et al., 2021). Yet, it can be skipped in the traditional interpretation of the seismic amplitude data. Consequently, several interpretation workflows were developed using fault-enhancement attributes (Mora et al., 2022; Perico et al., 2023).

In the present work, we apply a high-resolution fault mapping workflow to map the subtle fault system at the Marlim field in the offshore portion of the Campos Basin (Figure 1). The proposed workflow comprises four main steps: data preconditioning, well-to-seismic tie, inversion for relative acoustic impedance estimation and advanced fault attribute applications. As a result, we imaged two distinct fault distributions inside and outside the main reservoir.

GEOLOGICAL SETTING

Like all other basins on the Brazilian eastern margin, the Campos Basin was formed due to the distension process that began in the Middle Jurassic during the fragmentation of the supercontinent Gondwana. The rifting process resulted in the formation of antithetic and synthetic normal faults, accommodation zones and transfer faults. This fault system configured the compartmentalization of the Precambrian basement into a series of horsts and graben, with a structural pattern of rotated blocks, informally known as domino style. The Rifting events began in the Eocretaceous, more precisely in the Hauterivian, as evidenced by the 135-124 Ma basalts of the Cabiúnas Formation (Mizusaki et al., 1992).

In this tectonic context, sediments from the Rift megasequence were deposited, predominantly alluvial and deltaic clastics in the proximal areas, with lacustrine clay deposits filling the lowest points and bioclastic bars covering the highest isolated points (Figure 2). The subsidence process was intensified from the Buracica Floor, Upper Barremian (Chang et al., 1992), forming lower deposition points at greater depths. Guardado et al. (2000) state that the sedimentary environment evolved from a freshwater lacustrine environment during the Andar Buracica to a brackish to saline lacustrine environment in the Andar Jiquiá (Eo-Aptian). The primary hydrocarbon source rocks of the basin, the Buracica and Jiquiá shales of the Coqueiros Formation, were deposited in the lowest structural areas of this rift phase. The highest structural areas were deposition sites, mainly for coquinas rich in pelecypods and microbial carbonates, where the main pre-salt reservoirs were configured (Dias et al., 1990).

From the Alagoas Floor (Aptian), mechanical subsidence ceased and thermal subsidence began, a process that resulted in tectonic quiescence. Subsequently, sediments from the Transitional Sequence were deposited, significantly contributing to siliciclastic sediments in the proximal areas and the development of microbial carbonates in the highest structural areas. With the development of the oceanic crust, the environment evolved into a hypersaline gulf system, which experienced sporadic communication with the open ocean and generated the deposition of evaporite rocks, the main seal of the basin. This gulf morphology evolved to open-ocean conditions, where a carbonate sedimentary environment was established during the Albian, with oolitic and oncolite bank alignments outlining thin micritic carbonates. An intense gravitational destabilization of the salt layer (halokinesis) occurred in the Mesoalbian, resulting in its eastward flow due to the tilt of the basin towards offshore areas. Halokinesis segmented the original continuous layer of salt in the nearest area, generating salt cushions that induced the formation of stripe faults, generating rollover-type structures, which favored the growth of thick carbonate banks. Salt displacement dragged overlying carbonate packages in the distal area, giving rise to raft-like structures marking a significant tectonic change in the basin (de Castro and Picolini, 2016).

Haq et al. (1987) describe a global rise in sea level in the Cenomanian that led to the drowning of the carbonate shelf, resulting in the deposition of a succession of calcilutites, shales, and subordinate sandstones. From the Turonian onwards, open sea conditions were established, with a depositional predominance of shale, mudstones and turbidites that were deposited preferentially during recurrent sea-level lows. An important sub-alkaline to alkaline magmatic event (de Castro and Picolini, 2016) occurred in the south of the basin between 83 and 45 Ma, resulting in diabase intrusive and basaltic extrusive bodies, as well as breccias and hyaloclastite, evidenced by packages of volcanic rocks proximal to the Cabo Frio High that decisively interfered in the structuring of the oil traps.

From the Eocene onwards, there was a significant increase in sedimentary influx and the consequent progradation of the proximal depositional environments towards the interior of the basin (Ribeiro et al., 2012), caused mainly by the reactivation of the source area, with the uplift of the Serra do Mar from the Cretaceous/Paleogene, resulting in the alignment of the interior grabens of São Paulo, Taubaté, Resende and Baixo Paraíba do Sul, allowing the capture of greater drainage directed to the Campos Basin, in addition to humidifying the climate. The deposition of important turbidite systems with clayey intercalations occurs in this context (Bruhn et al., 2003), especially in the Eocene, Oligocene, and Miocene, where faults and stratigraphic traps compartmentalized these sandstones from the Carapebus formation to a certain degree, characterized as the primary source of oil in the Campos Basin. Finally, the de-

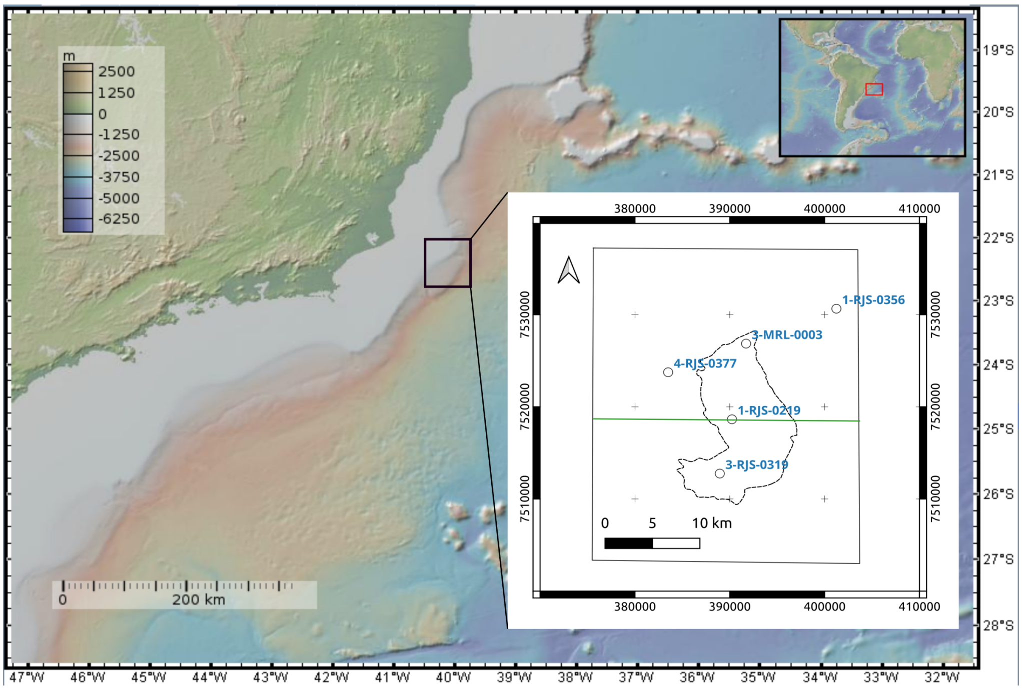

Figure 1: Location map of the Marlim field in Campos Basin. The inset shows the Marlim reservoir outline (dashed black line), five available wells (black and white circles) and the location of Inline 326 from the seismic cube (green line).

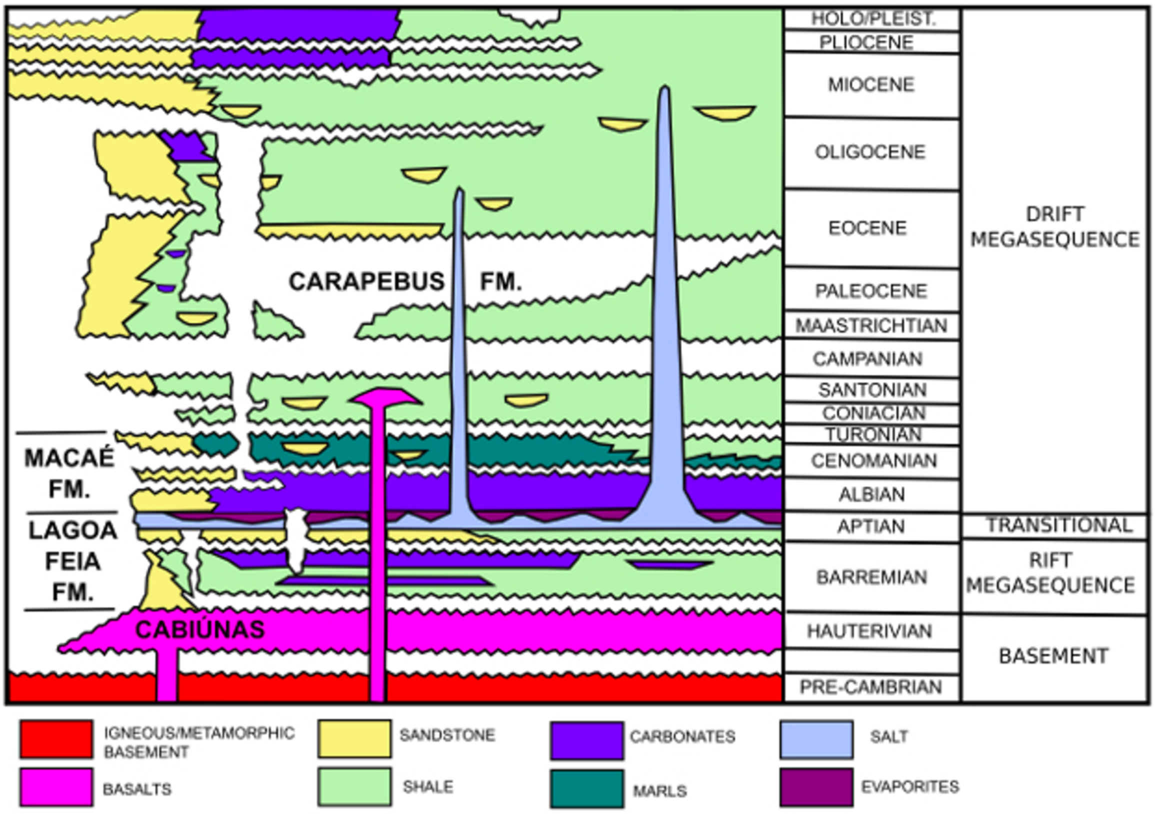

Figure 2: Simplified stratigraphic chart of the Campos Basin. Modified from Guardado et al. (2000).

position of a thick wedge of prograding sediments in deep waters occurred at the end of the Miocene, conditioned by the action of bottom currents, which altered the morphology of the central part of the basin to its current form, which allowed the accommodation of turbidites and generation of contemporary reservoirs (de Castro and Picolini, 2016).

MARLIM FIELD DATASET

The Marlim field, located offshore in the northeastern portion of the Campos Basin, was one of the largest oil field discoveries in 1985, with oil production commencing in 1991, when it became Brazil's largest producing field, with a daily production of 610,000 barrels (Johann et al., 2009).

The field comprises an Oligocene/Miocene deepwater turbidite system, forming the Marlim sandstone, a series of amalgamated sandstone bodies (Peres, 1993). A regional northwest-southeast transfer fault system influenced the turbidite sedimentation. This regional system was reactivated in the Tertiary, providing the pathway for the turbidite sedimentation in the Campos Basin (Cobbold and Meis, 2001). The Marlim trap is stratigraphic in the western, northern and southern regions. The trap is structural to the east, where the accumulation ends against a normal listric fault linked to the moving salt underneath. According to Mello et al. (1994) *apud* Nascimento et al. (2014), this fault is the primary route for oil migration from the pre-salt source rocks to the turbidite reservoir.

Geco-Prakla acquired for Petrobras the 3D seismic data analyzed in this project in 1997 (Johann et al., 2009). The acquisition parameters are shown in Table 1. This dataset became public in 2003 when the National Agency of Petroleum, Natural Gas and Biofuels (ANP) delivered a post-stack time-migrated, 3D seismic amplitude volume. ANP also provided data from five wells (Figure 1), including check shots, lithology, stratigraphic markers and composite well logs – density (ρ), sonic (DT), porosity (ϕ), and gamma-ray (GR) – in the Log ASCII Standard (LAS) format.

Table 1: Seismic acquisition parameters at Marlim field.

Marlim 3D acquisition	
Number of cables	6
Channels/cable	288
Shot point interval(m)	25
Receiver interval (m)	12.5
Cable interval (m)	50
Sample rate (ms)	1
Bin size (m)	12.5x25
Cable depth (m)	9
Inlines Azimuth (°)	123
Nominal fold	73
Traces/km^2	230400
Survey area (km^2)	720

FAULT MAPPING WORKFLOW

Figure 3 shows the four-step workflow used to interpret the Marlim seismic data, namely, by (1) data preconditioning, (2) well-to-seismic tie, (3) relative impedance estimation and (4) fault likelihood attributes applied to the inverted data.

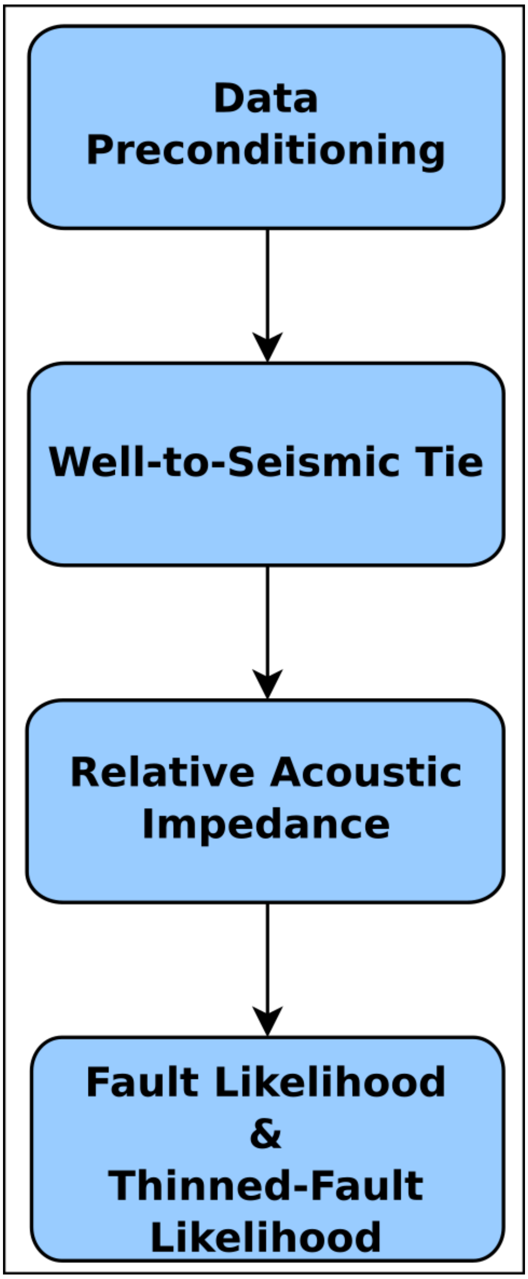

Figure 3: Schematic diagram of the presented four-step workflow.

In the first step, called data preconditioning, our goal is to reduce the random noise present in the dataset to prevent the noise from being enhanced during the acoustic inversion process. The second step, called well-to-seismic tie, links the information from the well-log to the interpreted seismic reflections, making it possible to identify specific horizons accurately. Additionally, this step estimates the seismic wavelet used in the acoustic impedance inversion utilized in the third step. Finally, the fourth step involves using modern seismic attributes to the relative impedance data to improve interpretation by identifying faults and fault zones.

Data preconditioning

Seismic Data

Seismic inversion methods depend on the seismic data quality and resolution (da Cunha et al., 2019). Often, even a small amount of noise spoiling the amplitude data can disguise subtle reflections. Hence, data filtering is required to reduce noise and enhance the seismic data signal-to-noise ratio.

We applied a dip steering median (DSM) filter (Qayyum and de Groot, 2012) to attenuate the high-frequency random noise from the seismic amplitude data. The main advantage of the proposed approach is that the median operator removes outliers in the data and retains steps in data values as encountered in nearby faults. Hence, the filtering procedure maintains the amplitudes and edges of the traces and enhances them as continuous events (Qayyum and de Groot, 2012). Therefore, it simplifies structural interpretation by enabling more accurate horizon auto-tracking and permitting the interpreter to extract more detail from the seismic data.

Figure 4 shows the comparison between the original seismic amplitude data (upper panel) and the DSM-filtered data (lower Panel). In the filtered data, it is possible to observe an overall improvement associated with the high-frequency noise content reduction. As a result, we obtain a sharper subsurface image. An important aspect of the filtered data is the better definition of small amplitude reflections between the major horizons. The enhancement of the lateral continuity of these small reflections is necessary for a precise structural horizon interpretation. According to Brouwer et al. (2012), using smoothed dip fields is preferable because they are more continuous than amplitude fields and less noise-prone.

After filtering the data, we significantly improved the seismic image by reducing high-frequency noise content, evidenced by their amplitude spectrum, as shown in Figure 4. In the filtered data, frequencies higher than 70 Hz are attenuated considerably in the DMS-filtered data, resulting in a clearer subsurface image (see the lower panel of Figure 4).

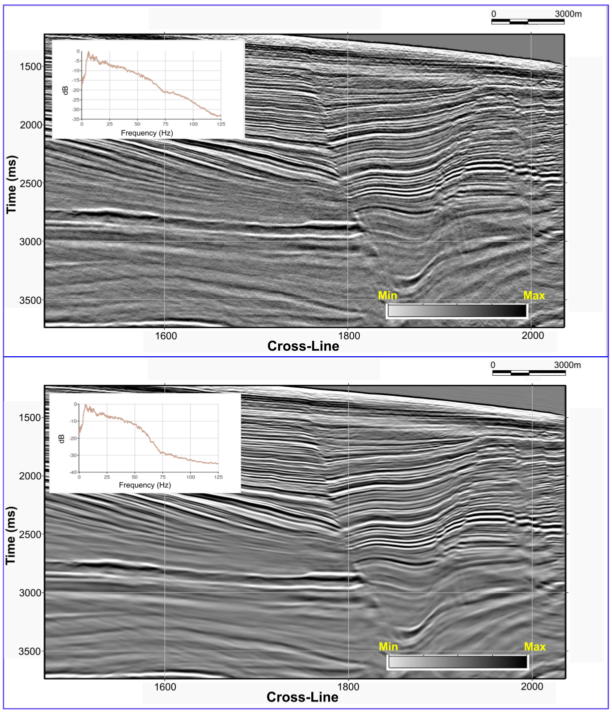

Figure 4: Noise attenuation results shown zoomed at the central portion of the Inline 326 (location in Figure 1) with corresponding spectra. Upper panel - The original amplitude data. Lower panel – Seismic dataset after the Dip Steered filter.

Well Data

The well data were uploaded into the seismic interpretation platform, and the logs were edited using the following steps:

1. Data Quality Check: This step involves confirming the integrity of the log data files to ensure completeness and removing artifacts or anomalies.

2. Log Splicing and Merging: Data from distinct runs or different logging tools were merged to create a continuous log profile for each well, describing subsurface properties without gaps or discontinuities in the logged interval.

3. Depth Alignment: This step ensured all logs were appropriately aligned at the same depth references, such as the total depth or specific depth markers of the well. This alignment enabled accurate correlation and comparison of the logs across different wells or intervals.

4. Data Cleaning: In this step, the log data were checked for noticeable errors, spikes, or outliers. These points were identified and removed.

Well-to-Seismic-tie (WST)

Synthetic seismograms generated from well logs(WST) best relate the seismic response to rock properties (Figure 5). It is widely used for seismic interpretation as they allow the correct labeling of picked seismic reflections and optimizes the correlation between an acoustic impedance model and the seismic data. A successful inversion strategy begins with wavelet estimation via WTS at all appropriate wells. After that, the estimated wavelet is cross-correlated and validated to invert the seismic data. Usually, the correlation rate of the WTS relies on the quality of the logs and seismic data and the time-to-depth relationship at a given well (Nascimento et al., 2014).

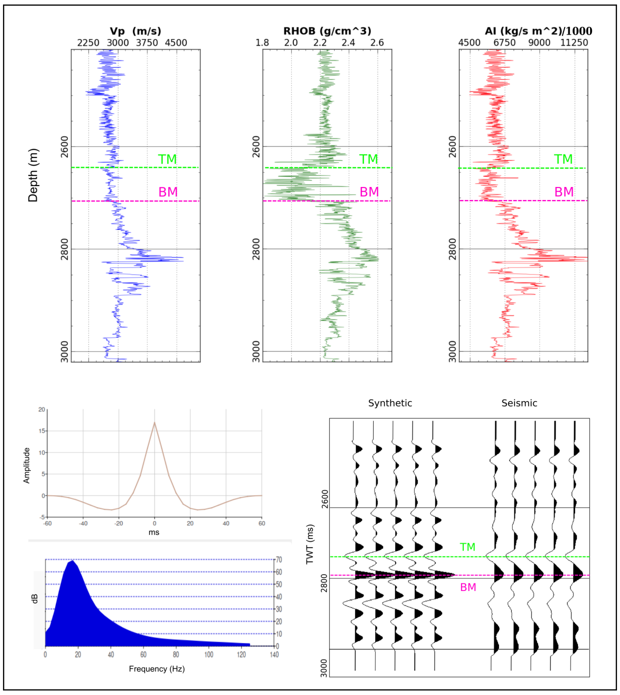

Figure 5: Well-tie correlation panel for the 1-RJS-0219 well. Upper panel - Vp Sonic (blue curve), density logs (green curve) and acoustic impedance log (red curve). Lower right panel - extracted wavelet and its frequency content. The lower left panel compares the synthetic and acquired seismic with the markers overlaid. TM is the top of the Marlim reservoir marker; BM is the bottom of the Marlim reservoir marker.

The well-to-seismic tie is a valuable method for connecting seismic response to rock properties using synthetic seismograms generated from well logs. This technique is widely used in interpretation because it accurately identifies mapped seismic reflections and optimizes the correlation between the acoustic impedance model and seismic data. A comprehensive review of the well-to-seismic good practices is found in the tutorial of White and Simm (2003).

The first step to creating a successful inversion scheme is determining the wavelet for a well-to-seismic tie at all appropriate wells. Once generated, cross-correlation and validation can be used to select the best wavelet for inverting the seismic data. The correlation rate for the seismic-to-well tie typically depends on the quality of the well and seismic data, as well as the time/depth relationship. We applied the process to all five wells; Figure 5 shows the results at the 1-RJS-0219 well (location in Figure 1).

We calculated the acoustic impedance (AI) log using the following relationship: AI $= \rho$V, the P-wave velocity log computed from the sonic log (V=1/DT). Next, we established the well-to-seismic tie in time by extracting a statistical wavelet from the data. The goal was to estimate a wavelet to increase the correlation between the synthetics and the seismic data. We extracted the wavelet utilizing a 500 ms window centered at 2650 ms. We then convolved the impedance log with the extracted wavelet to compute the synthetic data. The correlation between the synthetic and actual seismic data was 83%, consistent across all five wells in the study area (Figure 5).

According to Nascimento et al. (2014), two geologic factors can explain the 17% mismatch between the seismic and synthetic data. We have a dipping siliciclastic sequence above the top of the Marlim reservoir horizon(TM), which is a 2D situation, whereas the convolutional model is essentially 1D. Below the Marlim reservoir base (BM), heterogeneous carbonate units occur that can lead to a lower correlation between the signals.

S3-Relative Impedance Inversion

The seismic inversion process involves retrieving the subsurface impedance model or other elastic properties from seismic data (Nascimento et al., 2014). One method commonly used is formulating a solution by minimizing an objective function that defines the difference between the observed and modeled seismic data (da Cunha et al., 2019). However, the stationary convolution model fails to consider propagation effects like absorption and dispersion on actual seismic data.

We adopted the continuous wavelet transform (CWT) inversion scheme that Braga (2011) developed to compute the relative acoustic impedance, which has arbitrary amplitudes that show depth-dependent variations equivalent to those exhibited by log data. The inversion scheme herein adopted brings the benefit of the ability of the continuous wavelet transform (CWT) to represent a nonstationary phenomenon (Appendix A). Figure 6 shows an example of the inverted data.

High-Resolution Fault Mapping

Identifying the natural faults and fracture systems within hydrocarbon reservoirs can positively impact production and avoid geohazard problems during drilling operations (Coelho et al., 2021; Rocha et al., 2022; Perico et al., 2023). Geoscientists have dedicated substantial effort to designing seismic attributes to better map faults for several decades (Hussein et al., 2021; Ferreira and Porsani, 2023). One of the first was the development of coherence attributes that quantify lateral changes in the seismic amplitude and/or waveform (Bahorich and Farmer, 1995). Spectral decomposition is another technique used for fault identification by emphasizing the spectral phase components (Partyka et al., 1999) or using a red-green-blue blending of the spectral magnitudes (Henderson et al., 2008). Geometric attributes, like dip and curvature, have been developed to illuminate small faults and fractures (Roberts, 2001). Hale (2013) proposed an efficient algorithm to calculate, from seismic volumes, images of fault likelihood, strikes and dips.

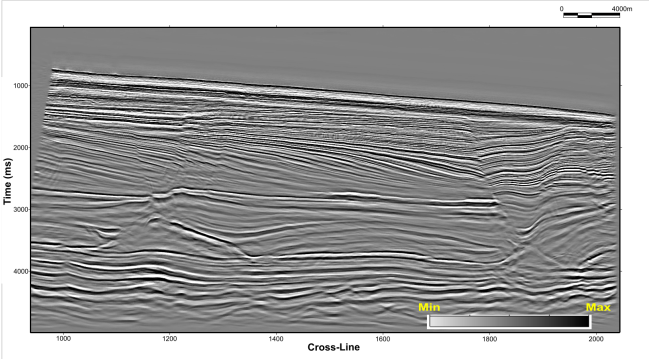

Figure 6: Inline 326. Relative acoustic impedance attribute.

We applied the Fault Likelihood (FL) and its derivative Thinned Fault Likelihood attributes (Hale, 2013) to improve fault mapping efforts to the relative acoustic impedance volume. Fault attributes are typically determined using semblance, coherence, or discontinuity analysis, which assumes that faults may exist in areas of low continuity in seismic reflections or high discontinuity. The FL attribute is designed to identify and outline faults and fractures in seismic data, providing a probability of their occurrence. The TFL is calculated using semblance power directly applied to the seismic dataset (Wu and Hale, 2016). We applied a localized Velocity Fan filter to attenuate and remove artifacts from FL and TFL attributes. This 3D f-k filter smooths the input at every sample position by filtering along velocity lines (van Hout, 2022). The final results are shown in Figures 7 and 8.

DISCUSSION

According to Bruhn et al. (2003), oil accumulations in turbidite reservoirs occur predominantly through structural control of faults, concentrated in the underlying upper Aptian evaporites or linked to the Precambrian basement. The role of faults is fundamental to the compartmentalization of reservoirs and providing conduits for the migration of petroleum from the underlying rift phase source rocks. Most of these reservoirs also have a certain degree of stratigraphic control, either by the clamping of the reservoir and/or the partial erosion of the reservoir by younger, mud-filled channels.

Figure 7 shows the FL attribute superimposed on the relative acoustic impedance along Inline 326. We can observe two salt domes that are central elements of the salt movement process, which functioned as central elements of the mass movement process, resulting in the basin accommodation process that resulted in the generation of two main synthetic faults generated by adiastrophic tectonics that acted in the compartmentalization of the Marlim reservoir, one to the west and the other to the east of the reservoir, positioned precisely above the fault region. The faults were followed by an accommodation sequence generating synthetic and antithetic secondary faults on both sides and always east of the main fault.

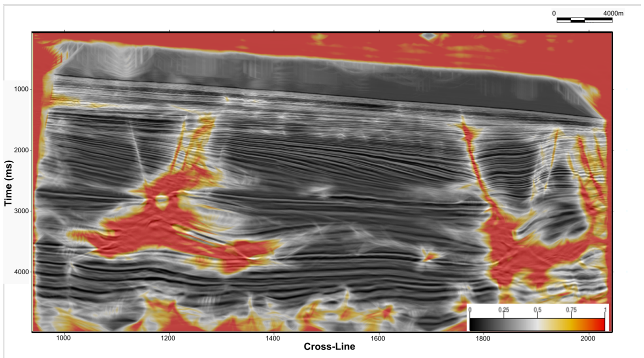

Figure 7: Inline 326. The fault likelihood attribute is superimposed on the relative acoustic impedance attribute.

Figure 8a shows the original seismic amplitude as provided by ANP. This is the starting point of our workflow. Some major faults outside the Marlim reservoir are visible in the original data, but inside the reservoir, the responses of the faults are masked within the reservoir amplitudes.

Figures 8b and 8c display the FL and TFL attributes extracted on the top of the Oligocene Horizon, which encompasses the Marlim turbidites. The seismic attribute revealed several subtle faults not observed in the seismic amplitude attribute. Moreover, the resulting images indicate that the Oligocene horizon can be divided into two regions with distinct fault trend characteristics, inside and outside the reservoir, confirmed by the rose diagrams of Figure 9.

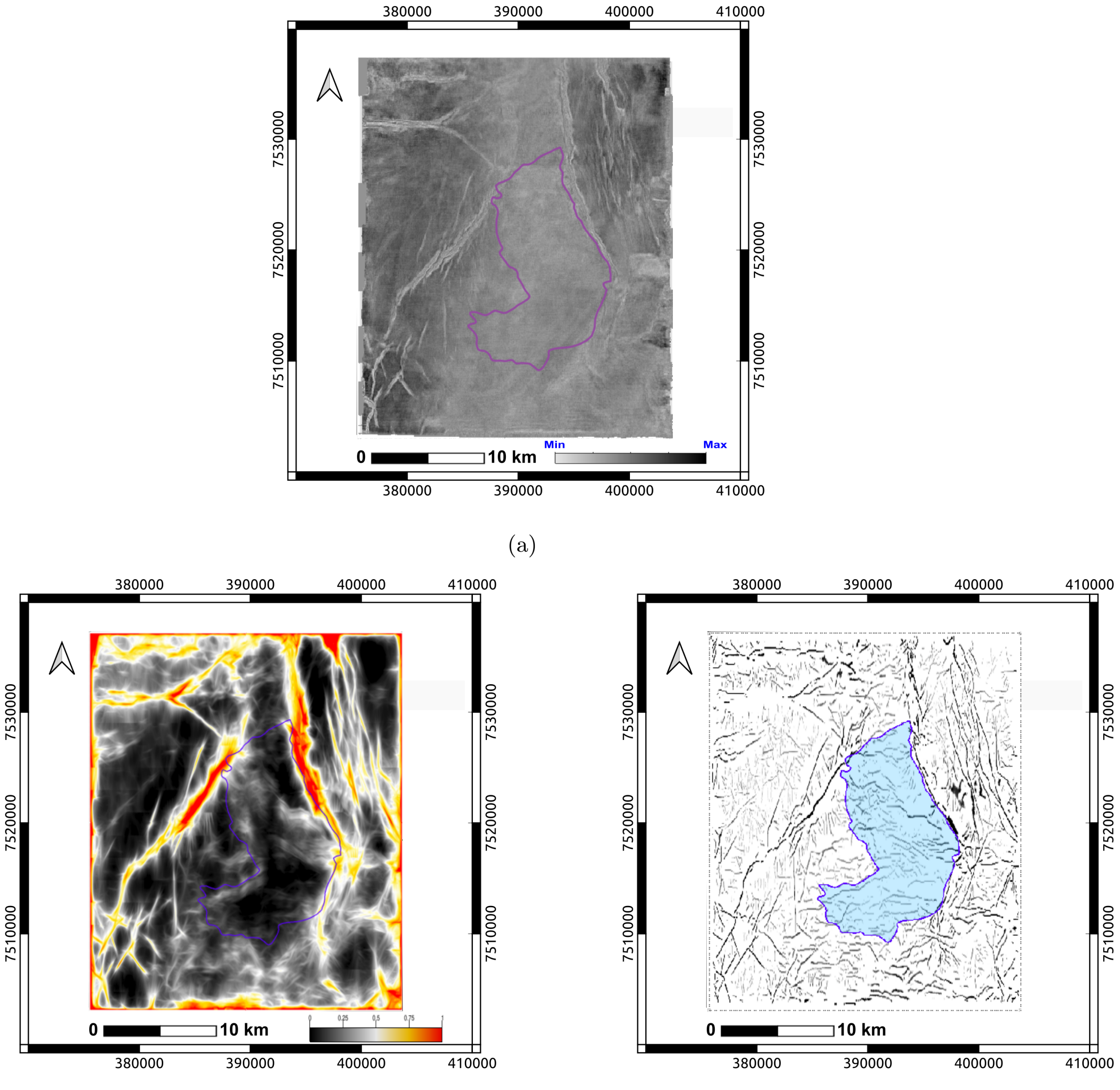

(a)

(b)

(c)

Figure 8: Seismic attributes extracted on the top of the Marlim Oligocene horizon. (a) Original seismic amplitude attribute; (b) Fault likelihood attribute; (c) Thinned-fault likelihood attribute. The Marlim reservoir outline is the purple line.

Outside the reservoir, the large faults trend to an average north-south direction. In contrast, the subtle faults and fractures in the reservoir present average east-west directions with a slight azimuthal inclination to the northwest. The interpreted fractures coincide with the higher porosity zones, above 30%, defined by Nascimento et al. (2014), indicating the importance of these fractures in the reservoir facies distribution.

The two fault patterns present behaviors that are approximately orthogonal to each other. This aspect may be related to the distinct rheological behavior in these domains, as it is likely to have been conditioned by the movement of the underlying salt, which generated a different stress regime within the reservoir to its envelope.

By analyzing this result, we can infer that the presence and movement of salt and faults influenced the fault distribution at the Marlim reservoir. Additionally, the burial of recent layers played an important role in controlling the direction of subtle faults and fractures within the reservoir.

CONCLUSION

This paper presents a seismic interpretation workflow to improve reservoir characterization by mapping subtle faults and fractures in a given area. The proposed workflow includes dip-steered spatial filtering, Well-to-seismic ties, relative acoustic impedance estimation and specialized fault attribute extraction applied to the relative acoustic impedance attribute.

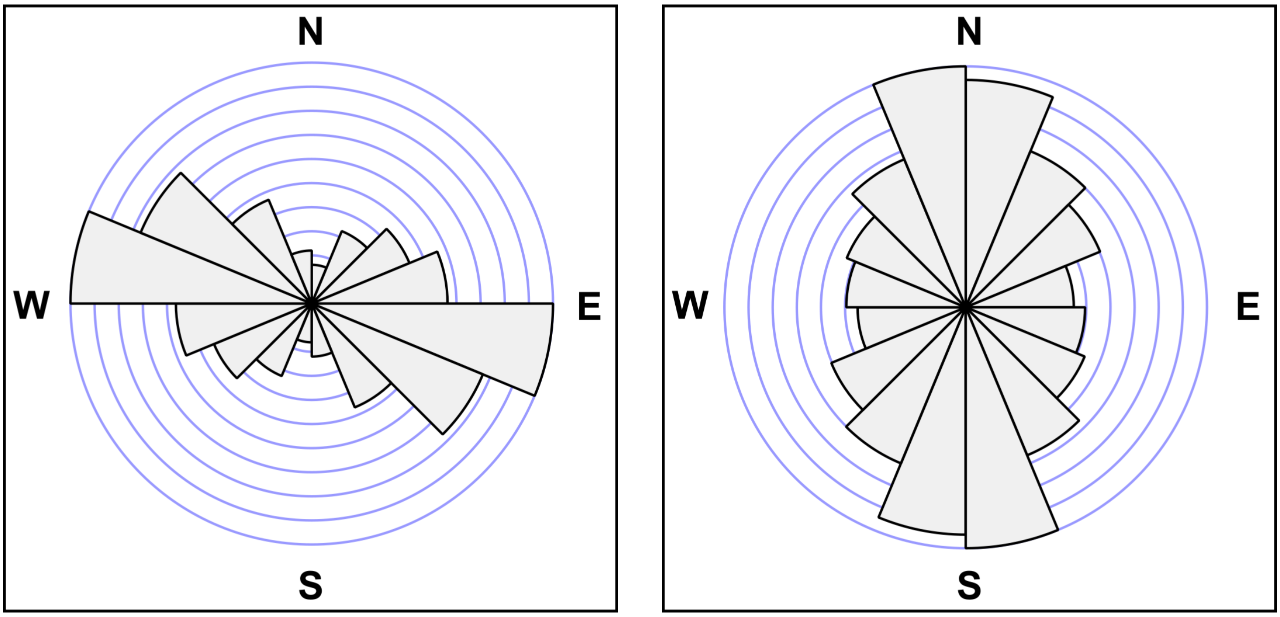

(a) (b)

Figure 9: Rose diagrams generated from the Thinned Fault Likelihood attribute on the top of the Oligocene Horizons. (a) Fractures inside the Marlim reservoir; (b) Faults and fractures outside the Marlim reservoir.

Dip-steered spatial filtering notably decreases the seismic data noise, permitting relative acoustic impedance inversion with greater accuracy and decreasing noise to a reasonable level. Using the fault likelihood and the thinned-fault likelihood attributes in the relative acoustic impedance data allowed the identification of the fault trends in the studied area.

The workflow was applied to Marlim, a mature field in the Campos basin. As a result, we imaged the fault distribution along the Oligocene horizon, separating it into two main regions with distinct fault densities and directions outside the reservoir characterized by large fault zones trending NNE-SSW and minor fractures inside the reservoir with an ENW-WSE trend.

Finally, we can suppose that the fault distribution of the Marlim reservoir was directly related to the presence and movement of salt, together with the burial of the most recent layers, in a way that also controlled the direction of subtle faults and fractures within the reservoir.

APPENDIX A. CWT INVERSION

Braga (2011) proposed a method that uses a series of filters in the wavelet domain to implement trace operations efficiently. In this method, a seismic trace $s(t)$ is considered a function of time and its Fourier transform $\widehat{s}(f)$ is a complex function of frequency f. The convolutional model represents the seismic trace as the convolution of the reflectivity series and a wavelet function. The proposed method aims to develop a deconvolution filter in the wavelet domain. The Morlet wavelet is a suitable choice for the spectral decomposition of the seismic signal and it can be expressed analytically in the time and frequency domains as a pair of Fourier transforms:

$$\psi(t) = \frac{1}{\pi^{1/4}} e^{i2\pi f_0 t} e^{-t^2/2} \Leftrightarrow \psi(f) = \frac{1}{\pi^{1/4}} \sqrt{2} e^{-1/2(2\pi f - 2\pi f_0)^2}, \tag{A1}$$

where f_0 is a fixed parameter representing the wavelet center frequency. The wavelet transform of the seismic trace $\tilde{s}(\tau, \alpha) = W_s(\tau, \alpha)$ is a complex function of time τ and a scale α characterized by $\alpha = f/f_0$. The continuous wavelet transform (CWT) can be defined as the inverse Fourier transform of the product of $\widehat{s}$ and $\widehat{\psi^*}$ (Addison, 2017):

$$\tilde{s}\,(\tau, \alpha) = \sqrt{a} \int_{-\infty}^{\infty} \widehat{s}(f) \widehat{\psi}^* \alpha e^{i2\pi f \tau} df, \tag{A2}$$

where $\widehat{s}$ and $\widehat{\psi}^*$ are the Fourier transform of the input seismic trace s(t) and the complex conjugate of the Morlet wavelet, respectively.

Braga (2011) defines the nonstationary filter $G(f, t)$, function of time and frequency, to designate the relationship between the representation of the CWT and the nonstationary filters. An example is a nonstationary wavelet operating in a reflectivity series expressed by s(T). Assuming $\widehat{s_0}(t)$ as the Fourier transform of the reflectivity series and by using the nonstationary filter G and the inverse Fourier transform, we get

$$s_0(t) = \int_{-\infty}^{\infty} \widehat{s_0}(t) G(f,t) e^{i2\pi f t} df. \qquad \text{(A3)}$$

We can use the inverse filter $G^{-1} \equiv \Theta(\tau, \alpha)$ in the wavelet domain to recover the original reflectivity series $s_0(t)$. Then, we can obtain the expected output $s_0(t)$ without the effect of a transient wavelet through the inverse wavelet transform Addison (2017):

$$s_0(t) = \frac{1}{c} \int_{\alpha} \int_{\tau} \widehat{s_0} \Theta\left(\tau, \alpha\right) \psi_{(\tau,\alpha)} t \frac{d\tau d\alpha}{\alpha^2}, \qquad \text{(A4)}$$

where c is the normalization constant to counterbalance the wavelet energy. In practice, the spectral representation is redundant in time and frequency because the CWT is nonorthogonal. This redundancy allows inverse transform computation by summing the real part at all frequencies (Torrence and Compo, 1998).

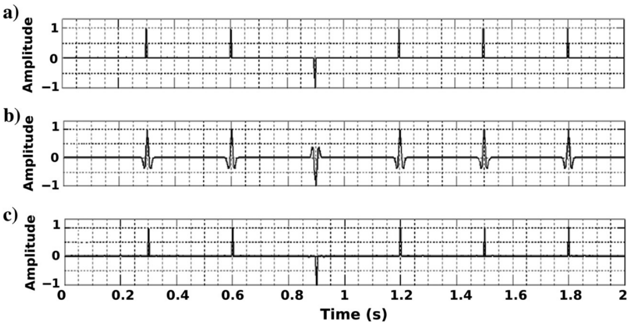

Figure A1: Retrieving of a reflectivity series via wavelet transform. (a) original reflectivity series; (b) seismic trace produced by the convolution of the original series of Figure 6a with a 40-Hz wavelet; and (c) recovered reflectivity series after using the inverse wavelet transform. Modified from Braga (2011).

The wavelet transform process through deconvolution is depicted in Figure A1, which shows an accurate recovery of the original reflectivity series, which can be confirmed by comparing the original (Figure A1a) with the retrieved one (Figure A1c). Once the reflectivity is recovered, the impedances can be easily calculated by integrating the trace (Braga, 2011).

ACKNOWLEDGMENTS

The authors are grateful to the BrJG Associate Editor and two anonymous reviewers for their valuable suggestions, which helped improve the text. The authors thank Cícero Regis for providing the BrJG latex template and dGB Earth Sciences for making the open-source seismic interpretation software OpendTect freely available. Data sets were made available by ANP under the support of the CNPq Project coordinated by Alexandre Evsukoff. Leonardo João acknowledges an ANP scholarship.

DATA AND MATERIALS AVAILABILITY

The data used in the manuscript belongs to the ANP agency and may be requested for research purposes.

REFERENCES

Addison, P. S., 2017, The illustrated wavelet transform handbook: introductory theory and applications in science, engineering, medicine and finance: CRC Press.

Bahorich, M., and S. Farmer, 1995, 3-D seismic discontinuity for faults and stratigraphic features: The coherence cube: The Leading Edge, **14**, 1053–1058, doi: 10.1190/1.1437077.

Braga, I. L., 2011, Tecnicas multiespectrais aplicada a fluxos de inversao e caracterizacao de reservatorios de hidrocarbonetos: PhD thesis, Universidade Estadual do Norte Fluminense (UENF).

Brouwer, F., A. Huck, N. Hemstra, and I. Braga, 2012, Extracting full-resolution models from seismic data to minimize systematic errors in inversion: Method and examples: The Leading Edge, **31**, 546–554, doi: 10.1190/tle31050546.1.

Bruhn, C. H., J. A. T. Gomes, C. Del Lucchese, and P. R. Johann, 2003, Campos Basin: Reservoir Characterization and Management - Historical Overview and Future Challenges: Presented at the All Days, OTC. doi: 10.4043/15220-ms.

Carvalho, B. R., and P. T. L. Menezes, 2017, Marlim R3D: a realistic model for CSEM simulations-phase I: model building: Brazilian Journal of Geology, **47**, 633–644, doi: 10.1590/2317-4889201720170088.

Chang, H. K., R. O. Kowsmann, A. M. F. Figueiredo, and A. Bender, 1992, Tectonics and stratigraphy of the East Brazil Rift system: an overview: Tectonophysics, **213**, 97–138.

Cobbold, P. R., and K. E. Meis, 2001, Reactivation of an obliquely rifted margin, Campos and Santos basins, southeastern Brazil: AAPG Bulletin, **85**, doi: 10.1306/8626d0b3-173b-11d7-8645000102c1865d.

Coelho, A. C., P. T. Menezes, and M. A. Mane, 2021, Gravity data as a faulting assessment tool for unconventional reservoirs regional exploration: The Sergipe–Alagoas Basin example: Journal of Natural Gas Science and Engineering, **94**, 104077, doi: 10.1016/j.jngse.2021.104077.

da Cunha, C. A., L. T. D. Silva, N. S. M. D. Cruz, A. Damasceno, T. S. D. Oliveira, and A. Pimentel, 2019, High Resolution Impedance Inversion: Brazilian Journal of Geophysics, **37**, 461, doi: 10.22564/rbgf.v37i4.2022.

de Castro, R. D., and J. P. Picolini, 2016, Main features of the Campos Basin regional geology, *in* Geology and geomorphology: Elsevier, 1–12.

Dias, J. L., J. C. Scarton, F. R. Esteves, M. Carminatti, and L. R. Guardado, 1990, Aspectos da evolução tectono-sedimentar e a ocorrência de hidrocarbonetos na Bacia de Campos: Origem e evolução de bacias sedimentares, **2**, 333–360.

Ferreira, G. D., and M. J. Porsani, 2023, Detection of Discontinuities in Post-Stack 3D Seismic Data Using Inline and Crossline Filtering: Brazilian Journal of Geophysics, **40**, doi: 10.22564/brjg.v40i4.2182.

Grana, D., T. Mukerji, and P. Doyen, 2021, Seismic reservoir modeling: Theory, examples, and algorithms: John Wiley & Sons.

Guardado, L. R., A. R. Spadini, J. S. L. Brandão, and M. R. Mello, 2000, Petroleum system of the campos basin, brazil, *in* Petroleum Systems of South Atlantic Margins: American Association of Petroleum Geologists, 317–324. doi: 10.1306/m73705c22.

Hale, D., 2013, Methods to compute fault images, extract fault surfaces, and estimate fault throws from 3D seismic images: GEOPHYSICS, **78**, O33–O43, doi: 10.1190/geo2012-0331.1.

Haq, B. U., J. Hardenbol, and P. R. Vail, 1987, Chronology of fluctuating sea levels since the triassic: Science, **235**, 1156–1167, doi: 10.1126/science.235.4793.1156.

Henderson, J., S. J. Purves, G. Fisher, and C. Leppard, 2008, Delineation of geological elements from RGB color blending of seismic attribute volumes: The Leading Edge, **27**, 342–350, doi: 10.1190/1.2896625.

Hussein, M., R. R. Stewart, and J. Wu, 2021, Which seismic attributes are best for subtle fault detection?: Interpretation, **9**, T299–T314, doi: 10.1190/int-2020-0068.1.

Johann, P., R. Sansonowski, R. Oliveira, and D. Bampi, 2009, 4D seismic in a heavy-oil, turbidite reservoir offshore Brazil: The Leading Edge, **28**, 718–729, doi: 10.1190/1.3148415.

Lupinacci, W. M., L. d. M. S. Gomes, D. J. A. Ferreira, R. Bijani, and A. F. M. Freire, 2020, An integrated approach for carbonate reservoir characterization: a case study from the Linguado Field, Campos Basin: Brazilian Journal of Geology, **50**, doi: 10.1590/2317-4889202020190103.

Mizusaki, A., R. Petrini, P. Bellieni, P. Comin-Chiaramonti, J. Dias, A. De Min, and E. Piccirillo, 1992, Basalt magmatism along the passive continental margin of SE Brazil (Campos Basin): Contributions to Mineralogy and Petrology, **111**, 143–160.

Mora, J. P., H. Bedle, and K. J. Marfurt, 2022, Fault enhancement using probabilistic neural networks and Laplacian of a Gaussian filter: A case study in the Great South Basin, New Zealand: Interpretation, **10**, SC1–SC15, doi: 10.1190/int-2021-0127.1.

Nascimento, T. M., P. T. L. Menezes, and I. L. Braga, 2014, High-resolution acoustic impedance inversion to characterize turbidites at Marlim Field, Campos Basin, Brazil: Interpretation, **2**, T143–T153, doi: 10.1190/int-2013-0137.1.

Partyka, G., J. Gridley, and J. Lopez, 1999, Interpretational applications of spectral decomposition in reservoir characterization: The Leading Edge, **18**, 353–360, doi: 10.1190/1.1438295.

Peres, W. E., 1993, Shelf-Fed Turbidite System Model and its Application to the Oligocene Deposits of the Campos Basin, Brazil: AAPG Bulletin, **77**, doi: 10.1306/bdff8b6e-1718-11d7-8645000102c1865d.

Perico, E., H. Bedle, B. Buist, and A. C. Damasceno, 2023, Fault characterization in a postsalt reservoir interval, Jubarte Field (Campos Basin), using seismic attributes and machine learning: Interpretation, **11**, T199–T214, doi: 10.1190/int-2022-0061.1.

Qayyum, F., and P. de Groot, 2012, Seismic dips help unlock reservoirs: American Oil & Gas Reporter, **60**, 75–79.

Ribeiro, M. C. S., P. C. Hackspacker, L. F. B. Ribeiro, and J. C. Hadler Neto, 2012, Evolução tectônica e denudacional da Serra do Mar (se/brasil) no limited entre o Cretáceo Superior e Paleoceno, utilizando análises de traços de fissão e U-TH/HE em apatitas: Revista Brasileira de Geomorfologia, doi: 10.20502/rbg.v12i0.254.

Roberts, A., 2001, Curvature attributes and their application to 3D interpreted horizons: First Break, **19**, 85–100, doi: 10.1046/j.0263-5046.2001.00142.x.

Rocha, N. M., A. C. Coelho, and P. T. L. Menezes, 2022, A high-resolution fault assessment workflow for unconventional reservoirs exploration: A case study on the onshore Sergipe-Alagoas Basin, Brazil: Journal of South American Earth Sciences, **113**, 103641, doi: 10.1016/j.jsames.2021.103641.

Torrence, C., and G. P. Compo, 1998, A Practical Guide to Wavelet Analysis: Bulletin of the American Meteorological Society, **79**, 61–78, doi: 10.1175/1520-0477(1998)079<0061:apgtwa>2.0.co;2.

van Hout, M., 2022, Removing noise and artifacts from (Thinned) Fault Likelihood: https://www.dgbes.com/blog/functionality-features-and-workflows/removing-noise-and-artifacts-from-thinned-fault-likelihood.

White, R., and R. Simm, 2003, Tutorial: good practice in well ties: First Break, **21**, doi: 10.3997/1365-2397.21.10.25640.

Wu, X., and D. Hale, 2016, 3D seismic image processing for faults: GEOPHYSICS, **81**, IM1–IM11, doi: 10.1190/geo2015-0380.1.

João, L.C.: methodology, validation, writing—review and editing, manuscript published version approval; **Menezes, P.T.L.**: conceptualization, methodology, validation, writing—original draft preparation, writing—review and editing, manuscript published version approval; **Bergamaschi, S.**: methodology, validation, writing—review and editing, manuscript published version approval.

Received on November 22, 2023 / Accepted on March 19, 2024

Creative Commons attribution-type CC BY